



Cite this: *RSC Adv.*, 2021, 11, 31557

High-performance asymmetric supercapacitor based on $\text{CdCO}_3/\text{CdO}/\text{Co}_3\text{O}_4$ composite supported on Ni foam†

Rodrigo Henríquez, *^a Alifhers S. Mestra-Acosta, ^a Eduardo Muñoz, ^a Paula Grez, ^a Elena Navarrete-Astorga ^b and Enrique A. Dalchiele ^c

A $\text{CdCO}_3/\text{CdO}/\text{Co}_3\text{O}_4$ composite has been prepared on nickel foam through a combined hydrothermal-annealing method. An asymmetric hybrid supercapacitor (SC) device was assembled with this composite as the positive electrode and activated carbon was the negative electrode. The SC exhibited a high specific capacitance of 84 F g^{-1} @ 1 mA cm^{-2} , a maximum energy density of 26.3 W h kg^{-1} , and a power density of 2290 W kg^{-1} , along with a wide potential window of 1.5 V and long cycle life (92% after 6000 cycles). SCs assembled in series powered various light-emitting diodes and moved an electrical mini-motor.

Received 7th July 2021
Accepted 4th September 2021

DOI: 10.1039/d1ra05243h

rsc.li/rsc-advances

1 Introduction

The rapid development of civilization and the high rate of population growth has resulted in the increased consumption of resources and, therefore, the demand for energy in the 21st century, which has caused enormous research efforts related to energy conversion and storage.^{1,2} As such, better energy storage devices are in urgent demand.³ Of the electrochemical energy storage devices, supercapacitors (SCs) are known as the most promising due to their high power delivery density, rapid charge-discharge rate, long cycle life, and safety of operation.⁴⁻⁶ However, their low energy density is considered a major challenge since it restricts their applications.⁴

SCs are divided into electric double-layer capacitors (EDLCs) and pseudocapacitors.^{3,7} The EDLCs rely on the physical adsorption and accumulation of electrostatic charges at the electrode/electrolyte interface, while the pseudocapacitors utilize the reversible valence changes in electrode materials to store/release energy generated by redox reactions.^{3,7} In recent years, the combined advantages of capacitive (for a high power density) and faradaic (for a high energy density) mechanisms in one supercapacitor device have led to the coining of the term “hybrid supercapacitor”.^{3,7} Hybrid capacitors are the combination of an EDLC and a pseudocapacitor electrode in one SC.^{3,7}

Asymmetric SCs (ASCs) assembled using two dissimilar electrode materials in an aqueous electrolyte are a practicable way to improve the energy density by widening the operation voltage window.⁷ The fabrication of asymmetric/hybrid SCs is a promising approach for overcoming the shortfalls of a low energy density in supercapacitors.⁸

The performance of SCs is dependent on the intrinsic properties of active electrode materials.⁹ Electrochemical double-layer capacitors (EDLC) employ mainly carbon derivatives materials with high surface area per unit, such as activated carbon, carbon nanofibers, or carbon nanotubes.¹⁰ On the other hand, pseudocapacitors use hydroxides or metallic oxides, such as manganese oxide (MnO_2),¹¹ nickel oxide (NiO),¹² cobalt hydroxide $\text{Co}(\text{OH})_2$,¹³ ruthenium oxide (RuO_2),¹⁴ ferric oxide (Fe_2O_3),¹⁵ and conducting polymers or copolymers such as polyaniline (PANI), polypyrrole (PPy), or a combination of these.¹⁶ Electrodes composed of cobalt, cobalt oxide^{17,18} and these hybridized with property-complementary nanomaterials, *i.e.*, metals,¹⁸ carbon-based materials,¹⁹ sulfides, or conducting polymers²⁰ have provided high specific capacitances and excellent cyclability as materials in SCs. Another metal used in SCs is cadmium (Cd), providing capacitance values of 1190 mF g^{-1} when used as CdO .²¹ Moreover, it has been demonstrated that the specific capacitance of cobalt electrodes was improved when doped or mixed with cadmium to obtain a specific capacitance of 737 F g^{-1} at a current density of 1 A g^{-1} .²² In the last few years, studies were conducted on the CO_3^{2-} ion with transition metals in many electrochemical storage applications, such as manganese carbonate (MnCO_3) with a capacitance of 216 F g^{-1} in SCs, improving wettability and electrode stability,²³ and CoCO_3 in Li-ion batteries demonstrating better stability than Co_3O_4 .²⁴ Very recently, hydroxycarbonates with $\text{M}_2(\text{CO}_3)(\text{OH})_2$ stoichiometry (where M represents the metal cations of Ni, Fe, Cu, Co, Zn, *etc.*)

^aInstituto de Química, Facultad de Ciencias, Pontificia Universidad Católica de Valparaíso, Casilla 4059, Valparaíso, Chile. E-mail: rodrigo.henriquez@pucv.cl; Tel: +56 32 2274921

^bUniversidad de Málaga, Departamento de Física Aplicada I, Laboratorio de Materiales y Superficies (Unidad asociada al CSIC), E29071 Málaga, Spain

^cInstituto de Física, Facultad de Ingeniería, Herrera y Reissig 565, C. C. 30, 11000 Montevideo, Uruguay

† Electronic supplementary information (ESI) available. See DOI: 10.1039/d1ra05243h



have received considerable attention as electro-active materials for high-performance supercapacitors due to high theoretical capacitance and variable compositions. For instance, electrode materials, such as the $\text{MoS}_2/\text{NiCo}(\text{OH})_2\text{CO}_3$ composite (as a nanosheet-assembled 3D flower-like nanostructure),²⁵ nickel-cobalt-manganese ternary carbonate hydroxide (as ultrathin nanoflakes)²⁶ and dendritic $\text{Co}_3\text{O}_4@\text{Co}_2(\text{CO}_3)(\text{OH})_2$ nano-arrays,²⁷ have been reported to give high-performance energy storage devices.

Moreover, it has also been reported that electrodes composed of 3D structures integrated with nickel foam (NF) as the current collector, with a porous architecture design without additives or binders provide high specific capacitance values.²⁷

In this work, an asymmetric hybrid SC with high energy density was designed from a mixture of $\text{Co}_3\text{O}_4/\text{CdO}/\text{CdCO}_3@\text{NF}$ by means of direct growth without additives or binders on an NF substrate.

2 Experimental methods

2.1 Materials

Commercial nickel foam (thickness: 1.1 mm, volume density: 0.45 g cm^{-3} , average pore diameter: 13.1 mm, PPI: 95–110, porosity: 95%, specific surface areal density: $330 \pm 10 \text{ g m}^{-2}$) was supplied by Career Henan Chemical Co. Ltd. (China). Cobalt nitrate hexahydrate ($\text{Co}(\text{NO}_3)_2 \cdot 6\text{H}_2\text{O}$, $\geq 98.8\%$), cadmium nitrate hexahydrate ($\text{Cd}(\text{NO}_3)_2 \cdot 6\text{H}_2\text{O}$, $\geq 99\%$), urea ($\geq 99.5\%$), and sodium hydroxide (KOH , $\geq 90\%$) were purchased from Sigma-Aldrich (USA). Activated carbon (AC) ($\geq 99.5\%$), polyvinyl alcohol (PVA) (99%). Carbon nanotubes (CNT) were synthesized by the chemical vapor deposition technique (CVD) in a tube furnace, using a temperature of 750°C and C_2H_4 gas as raw material and carbon source, without additional catalysts. A cellulose paper (Merck) was used. All chemicals were used as received without further purification. Deionized (DI) water obtained through a Millipore system (Milli-Q) with a resistance of $\sim 18 \text{ M}\Omega \text{ cm}^{-1}$ was used in the reactions.

2.2 Synthesis of the $\text{CdCO}_3/\text{CdO}/\text{Co}_3\text{O}_4@\text{NF}$ electrode

The active composite material ($\text{CdCO}_3/\text{CdO}/\text{Co}_3\text{O}_4$) was synthesized directly on the nickel foam substrate through a hydrothermal-annealing process. First, the nickel foam was cut into disk-shaped pieces with a diameter of 1.31 cm (1.35 cm^2 of geometrical area). The foam nickel samples were washed in acetone for 10 min, and then etched in 1 M HCl for 10 min to remove the surface oxide layer, and finally rinsed several times with DI water. Further, in detail, 2 mmol of $\text{Co}(\text{NO}_3)_2 \cdot 6\text{H}_2\text{O}$, 2 mmol of $\text{Cd}(\text{NO}_3)_2 \cdot 6\text{H}_2\text{O}$, and 15 mmol of urea were mixed in 50 ml of deionized water; after 10 minutes of stirring, the obtained homogeneous reaction solution was transferred along with a piece of clean nickel foam into a Teflon-lined stainless steel reactor. It was sealed and maintained at 95°C for 8 h, and then allowed to cool to room temperature. The prepared sample was collected and rinsed with DI water several times. Then, the active material supported on the nickel foam was subjected to heat treatment at 450°C under an argon flow of 105 sccm for

3 h, to obtain the composite electrode. The resulting active material mass loaded onto the NF was about 8 mg.

2.3 Synthesis of the activated carbon@NF negative electrode

The preparation of the negative electrode has been carried out following a modified technique that had previously been reported.²⁸ The active material (AC) was mixed with CNT and PVA in the weight ratio of 80 : 5 : 15, respectively, using ethanol as a solvent to form a homogeneous slurry. First, the AC was mixed with the CNTs in an agar mortar until a homogeneous mixture was obtained, then the PVA and 1 ml of ethanol were added to this mixture to obtain the carbon-based slurry. Further, the 1.31 cm diameter nickel foam sample was dipped into this carbon ink for 1 hour. Subsequently, to evaporate the solvent, the electrode was dried at 78°C for 24 hours in an oven in air. The resulting electrode had a geometric surface area of 1.35 cm^2 and exhibited a mass of active material of 15 mg.

2.4 Morphological, structural, and surface chemistry characterization

The structural characterization of the composite material was carried out by X-ray diffraction (XRD) on a PANalytical X'Pert Pro automated diffractometer. Patterns were recorded in the Bragg-Brentano configuration using a monochromatic high intensity ($\text{Cu K}\alpha_1$) radiation. An X'Celerator detector with a step size of $0.017^\circ (2\theta)$ was used, and the working power was $45 \text{ kV} \times 40 \text{ mA}$. Field emission scanning electron microscopy (FE-SEM) images of the electrodes were obtained on a Helios Nanolab 650 Dual Beam equipment from FEI Company. The analysis of the chemical composition of the formed structures was carried out using X-ray energy dispersion spectrometry (EDS). The equipment used was a QUANTAX 200 model from Bruker with XFLASH (EDX coupled to SEM equipment: Hitachi SEM SU-3500 of variable pressure with a detector 410-M). Samples for TEM were prepared by removing the gridded nanostructured grown material with a scalpel, then they were collected and ultrasonically dispersed in 1 ml of ethanol. A small drop of the suspended solution was placed on a porous carbon film on a nickel screen and allowed to air dry. Transmission electron microscopy (TEM) and high-resolution transmission electron microscopy (HRTEM) images were obtained on a Talos F200X instrument.

The oxidation states of the chemical elements were studied via X-ray photoelectron spectroscopy (XPS) using an ESCA 5701 from Physical Electronics (PHI). An $\text{Mg K}\alpha$ radiation source (15 eV) with an operating power of 400 W in an ultra-high vacuum system at a base pressure of $\sim 1.3 \times 10^{-8} \text{ Pa}$ was employed.

2.5 Assembly of the asymmetric hybrid supercapacitor

The supercapacitor was built using a two-electrode Swagelok cell, with a $\text{CdCO}_3/\text{CdO}/\text{Co}_3\text{O}_4@\text{NF}$ disk as the positive electrode, a cellulose paper as a separator (3 M KOH as the electrolyte), and an AC@NF disk as the negative electrode, all these parts were sandwiched and mounted into the cell holder between two stainless steel electrodes and compressing by a spring.



2.6 Electrochemical characterization

The electrochemical behavior of the resulting supercapacitor was evaluated by cyclic voltammetry (CV), galvanostatic charge-discharge (GCD) measurements and electrochemical impedance spectroscopy (EIS) carried out at room temperature with an electrochemical workstation (PGSTAT 30 AUTOLAB). EIS measurements were performed by applying an AC voltage with 10 mV amplitude in a frequency range from 0.1 Hz to 100 kHz at open circuit potential. Equivalent circuit modeling of the EIS spectrum has been analyzed by the ZView Software.

The specific capacitance per unit mass C_m ($F\ g^{-1}$), energy density E ($W\ h\ kg^{-1}$), and power density P ($W\ kg^{-1}$) of the SC determined from the galvanostatic charge/discharge data were given by the following:^{3,25}

$$C_m = \frac{I \times \Delta t}{\Delta V \times m} \quad (1)$$

$$E = 0.5 C_m (\Delta V)^2 \times \frac{1000}{3600} \quad (2)$$

$$P = \frac{E \times 3600}{\Delta t} \quad (3)$$

where I (A) is the applied current, Δt (s) is the discharge time, ΔV (V) is the operating voltage window (excluding the IR drop) and m (g) is the mass of the active material.

The mass matching of the positive and negative electrodes, respectively, was decided using the capacitor charge balance principle ($Q^+ = Q^-$) in the steady-state as follows:²⁹

$$\frac{m_+}{m_-} = \frac{C_- \Delta V_-}{C_+ \Delta V_+} \quad (4)$$

where C and m are the specific capacitance and the mass of electro-active materials, respectively, and ΔV is the applied voltage window for the negative electrodes ($-$), as well the positive ones ($+$).

3 Results and discussion

The representative synthetic procedure of the $CdCO_3/CdO/Co_3O_4@NF$ hybrid electrode is depicted in Fig. 1. The inset of Fig. 1 shows digital photographs of pristine NF and composite@NF samples after the hydrothermal process and after the annealing step. The color changed from gray for NF, to an intermediate magenta color, to black for the resulting SC electrode.

3.1 Morphological and structural properties of the $CdCO_3/CdO/Co_3O_4@Ni$ foam electrode

The morphological properties of bare nickel foam and $CdCO_3/CdO/Co_3O_4@Ni$ foam samples have been investigated by SEM observations as displayed in Fig. 2. An SEM image of the nickel foam substrate is depicted in Fig. 2a, showing a 3D porous network structure with pore size diameters from 150 to 370 μm , supplying a large surface area for supporting active materials. Fig. 2b depicts SEM micrograph images of a sample that underwent the hydrothermal process, showing that the

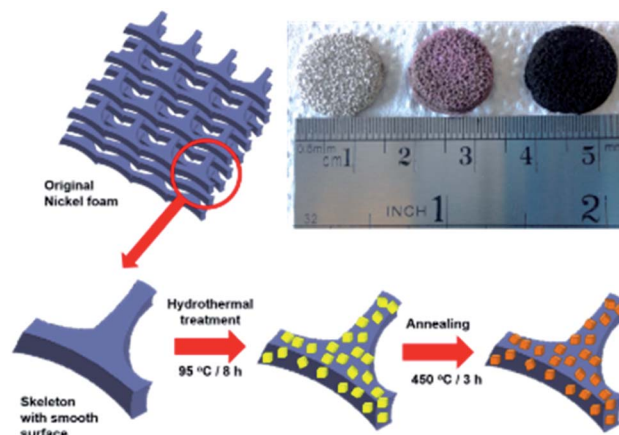


Fig. 1 Schematic illustration of the preparation process of the $CdCO_3/CdO/Co_3O_4$ composite on a 3D nickel foam electrode. The inset shows a digital photograph of a bare nickel foam sample (left), the sample after the hydrothermal step (center), and the resulting composite electrode after the annealing process.

composite densely and uniformly covers the skeleton surface of the nickel foam, with a high loading mass per NF real surface area of $4\ mg\ cm^{-2}$. It must be pointed out that this very good coverage is maintained even after the high-temperature annealing step. The composite material remained well adhered to the Ni foam substrate after being rinsed under centrifugation at a speed of 500 rpm for two minutes, indicating that it is an effective and robust binder-free integration. Fig. 2c and d show high magnification SEM micrographs of samples that underwent hydrothermal and hydrothermal plus high-temperature post-annealing processes, respectively. It can be seen that the composite consists of an agglomeration of micro-particles with cubic shapes, with an edge size of about 5–8 μm . The samples obtained after the hydrothermal process exhibited cubic particles with smooth surface faces (see Fig. 2c). However, in the samples that experienced hydrothermal and high-temperature post-annealing processes, the presence of roughness and nano-pores on the faces of the composite cubic micro-particles can be seen (see Fig. 2d). The presence of these nano-pores can be due to the evolution of the CO_2 product of the chemical decomposition of previously formed cadmium carbonate and the dehydration of cobalt hydroxide; both compounds were formed during the hydrothermal step process.

Fig. 2e shows a TEM image of a nano-portion of the $CdCO_3/CdO/Co_3O_4@Ni$ foam sample; Fig. 2f–h depict the corresponding EDS elemental mapping, revealing the presence of Ni, Cd, and Co elements in the sample. The high-resolution TEM image depicted in Fig. 2i (obtained from the zone indicated by a dashed rectangle in Fig. S1†), reveals three lattice fringes of 0.28, 0.24, and 0.46 nm, corresponding to the (104), (200), and (111) lattice planes of the rhombohedral phase of $CdCO_3$, the cubic phase of CdO and the cubic phase of Co_3O_4 (see ESI†). Fig. 2j depicts the corresponding fast Fourier transform (FFT) pattern of this HRTEM result. The very clear crystal lattice as well the corresponding well-ordered dot pattern of the FFT image demonstrated the high-quality single-crystalline nature



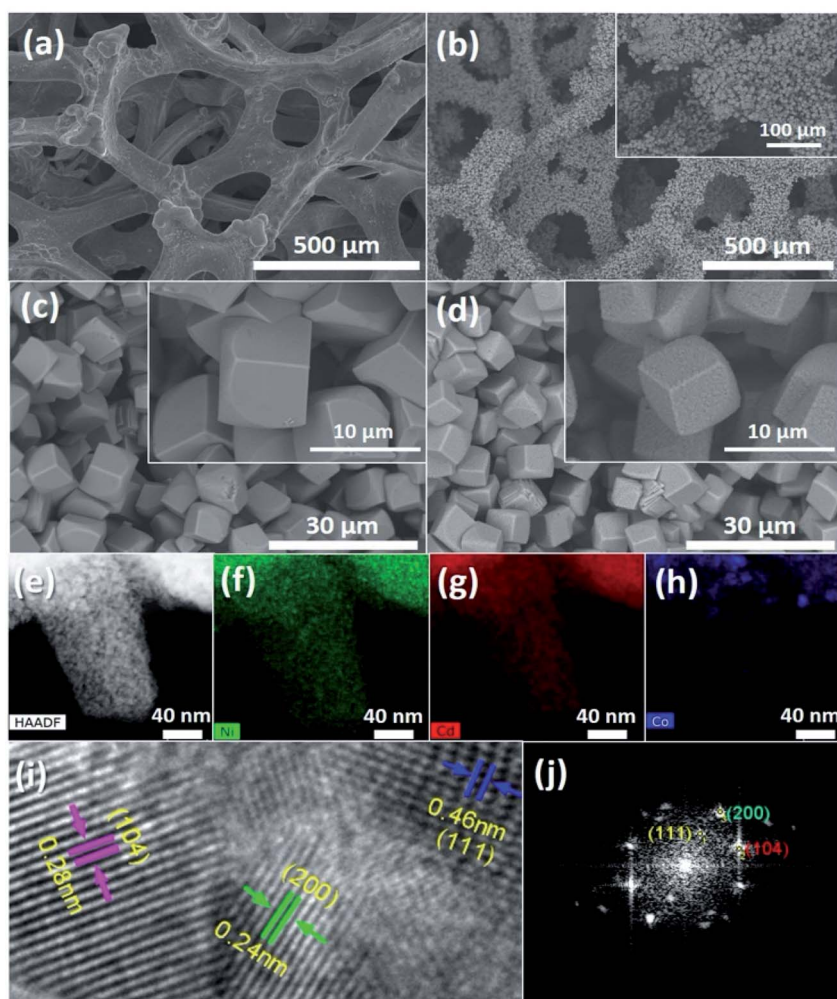


Fig. 2 SEM plane-view micrograph images of (a) the pristine nickel foam substrate and (b) the nickel foam after the hydrothermal process. SEM micrograph images depicting in more detail the cubic architectures exhibited by the $\text{CdCO}_3/\text{CdO}/\text{Co}_3\text{O}_4$ composites on nickel foam (c) after the hydrothermal process and (d) after an additional annealing treatment. The insets show high magnifications SEM micrographs. (e) TEM image of a nano-portion of nickel foam covered by the composite under study and the corresponding EDX elemental mapping of Ni (green), Cd (red) and Co (blue), depicted in panels (f), (g) and (h), respectively. (i) HRTEM micrograph of a $\text{CdCO}_3/\text{CdO}/\text{Co}_3\text{O}_4$ crystallite, lattice fringes corresponding to the involved chemical compounds are indicated; the corresponding FFT pattern is depicted in panel (j).

of the composite. However, structural analysis through XRD of the composite samples revealed only diffraction peaks corresponding to CdCO_3 and CdO phases, and those originated from the Ni substrate, and the lack of those corresponding to the Co_3O_4 phase (see Fig. S2 and S3[†]). EDS microanalysis results (see Fig. S4 and Table S1[†]) showed high oxygen and cadmium contents and low cobalt content. It must be pointed out that X-ray diffraction statistically gives us a good idea of the average sample, whereas electron diffraction in TEM allows us to obtain local structure information. It was inferred that there was a low quantity of the Co_3O_4 phase, which was formed by grains with small crystallite sizes, evidencing a low degree of crystallinity. XPS photoelectron spectroscopy analysis confirmed the presence of those compounds, see Fig. S5[†].

3.2 Supercapacitor electrochemical performance

To further evaluate the $\text{CdCO}_3/\text{CdO}/\text{Co}_3\text{O}_4/\text{Ni}$ foam hybrid electrode for real application, a 1.35 cm^2 ASSC device was made by using the $\text{CdCO}_3/\text{CdO}/\text{Co}_3\text{O}_4/\text{Ni}$ electrode as the positive one and the activated carbon (AC) film on Ni foam as the negative one in 3 M KOH with one piece of cellulose paper as the separator, (working potential is 1.5 V, see Fig. S6[†]), *i.e.*: the $\text{CdCO}_3/\text{CdO}/\text{Co}_3\text{O}_4/\text{Ni}/\text{AC}$ SC device. In the inset of Fig. 3, a scheme of the SC developed in this work shows the different components. To optimize the quantity of charge balance between positive and negative electrodes, the loading mass ratio between the $\text{CdCO}_3/\text{CdO}/\text{Co}_3\text{O}_4$ composite and AC electrodes was estimated by using eqn (4). According to this formula, the optimized mass ratio is ~ 0.43 . The mass values finally obtained were 8 mg and 15 mg for the positive and negative electrodes, respectively, leading to an optimized mass ratio of ~ 0.53 . The electrochemical performance of this ASSC



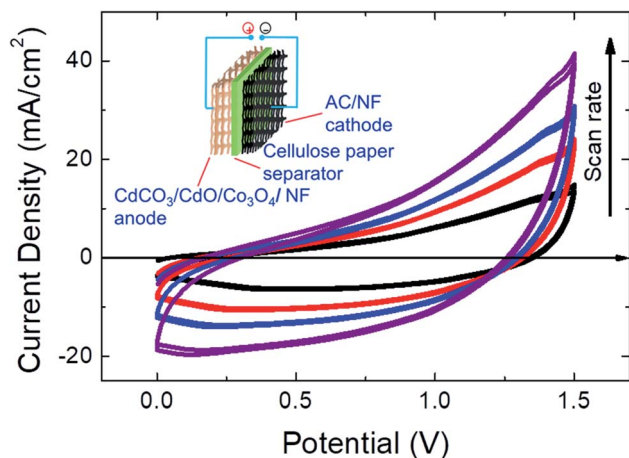


Fig. 3 Cyclic voltammetry of the $\text{CdCO}_3/\text{CdO}/\text{Co}_3\text{O}_4@\text{Ni}/\text{AC}$ supercapacitor device at different potential scan rates (10, 20, 30, and 40 mV s^{-1}). Inset: schematic diagram of the asymmetric supercapacitor configuration.

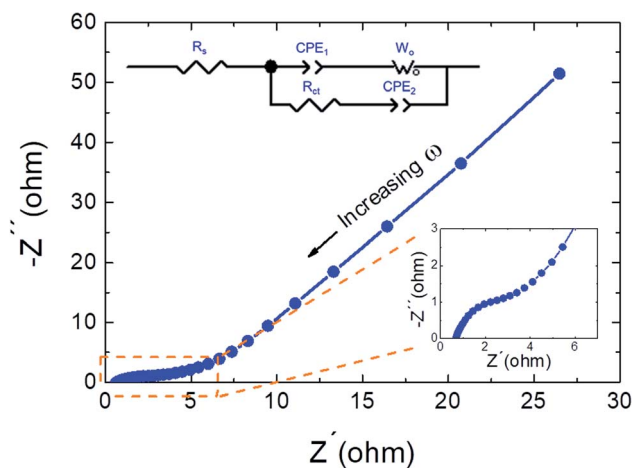


Fig. 4 Nyquist plot for the $\text{CdCO}_3/\text{CdO}/\text{Co}_3\text{O}_4@\text{Ni}/\text{AC}$ supercapacitor device at open potential conditions. The symbols (blue circles shapes) represent the experimental data; the blue line is the fitting result with the electrical circuit model. The upper inset shows the equivalent electronic circuit model used to fit the experimental EIS data, whereas the lower one shows an enlargement of the plot in the high-frequency range.

was investigated *via* two-electrode measurements. The cyclic voltammetric (CV) curves at various scan rates of the ASSC are shown in Fig. 3. The device exhibited a quasi-rectangular CV

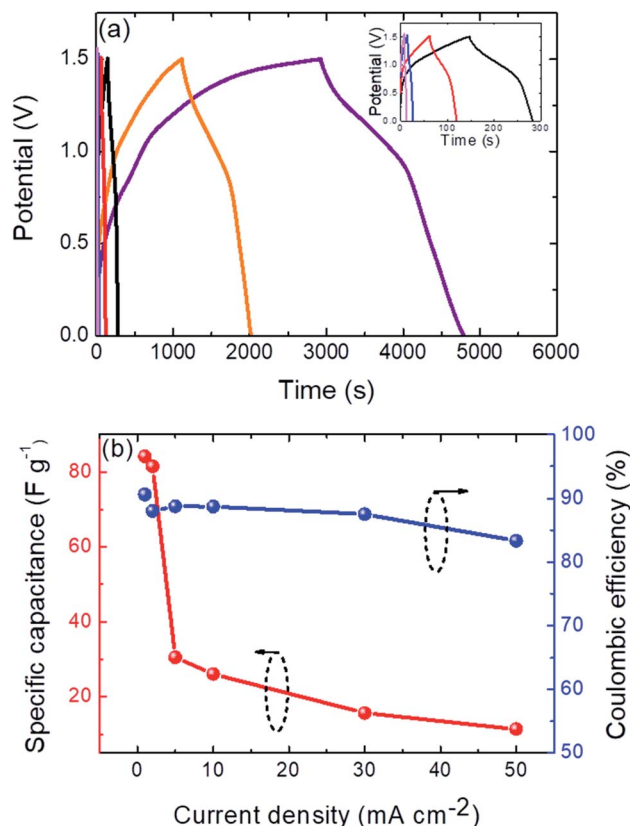


Fig. 5 (a) Galvanostatic charge and discharge of the $\text{CdCO}_3/\text{CdO}/\text{Co}_3\text{O}_4@\text{Ni}/\text{AC}$ supercapacitor device at different current densities: 1 mA cm^{-2} (purple line), 2 mA cm^{-2} (orange line), 5 mA cm^{-2} (black line), 10 mA cm^{-2} (red line), 30 mA cm^{-2} (blue line) and 50 mA cm^{-2} (light magenta line). For clarity, the curves corresponding to the highest current density values are depicted in the inset. (b) The rate capability and the coulombic efficiency of the $\text{CdCO}_3/\text{CdO}/\text{Co}_3\text{O}_4@\text{Ni}/\text{AC}$ supercapacitor device at different current densities.

shape. Even at high scan rates, the CV curves do not show obvious polarization, confirming that the cell potential of 1.5 V is reasonable.⁵ With the increasing scan rate, the shape of the CV curves remained unaltered and an increase of the device current was observed, which demonstrated the high rate capability of the device.⁶ This is indicative of an effective electric transport of ions onto the electrode surface. The large area under the curves revealed high capacitance values, as shown in Table S2,[†] for scan rates from 5 to 50 mV s^{-1} . Because of the mutual effect of the positive and negative electrodes, the operation potential window could reach as high as 1.5 V. The

Table 1 Equivalent circuit element values obtained through a complex non-linear least-squares fitting of the EIS spectra^a

R_s (Ω)	Q_1^b (Ss^{α_1})	α_1	R_{ct} (Ω)	Q_2^b (Ss^{α_2})	α_2	$W-R$ (Ω)	$W-T$ (s)	$W-P$
0.62	0.0028	0.60	4.32	0.025	0.64	24.07	0.18	0.9

^a See inset of Fig. 4 for the involved electrical equivalent circuit. ^b The impedance of a CPE is defined as $Z_{\text{CPE}} = \frac{1}{Q(j\omega)^\alpha}$, where α ($0 < \alpha < 1$) is an empirical constant with no real physical meaning.

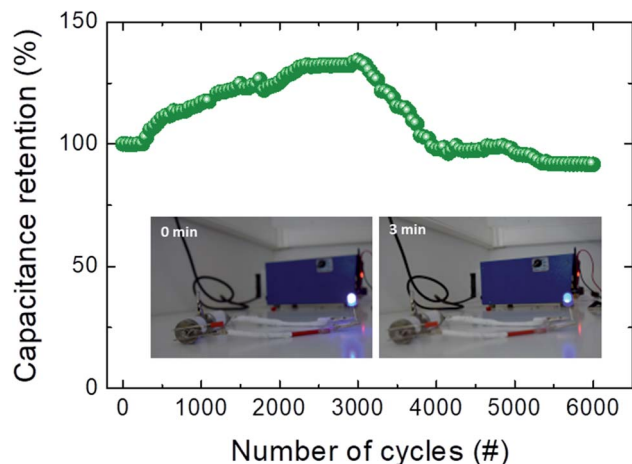


Fig. 6 Cycling stability of our device after 6000 cycles from an initial 84.0 F g^{-1} specific capacitance value. Inset: pictures showing that two SCs in series can light a blue LED indicator; the images show different stages powered by the SCs charged for 10 s.

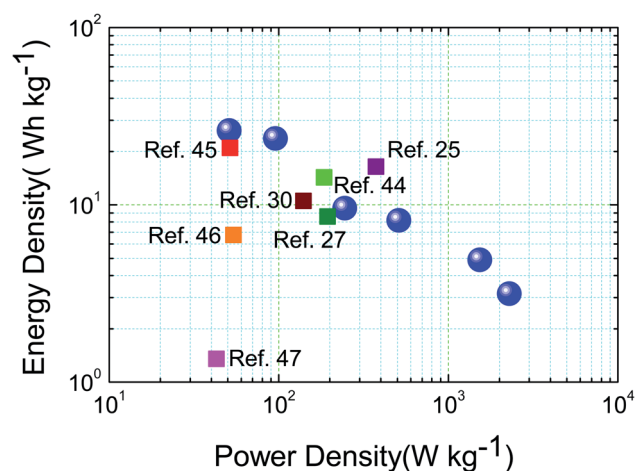


Fig. 7 Ragone plot of the hybrid $\text{CdCO}_3/\text{CdO}/\text{Co}_3\text{O}_4/\text{Ni}/\text{AC}$ supercapacitor device (blue spheres), and the main reported values in the literature.

potential window exhibited by this SC is higher than that observed in conventional symmetric SCs based on AC electrodes in aqueous electrolytes (0.8–1.0 V),^{7,8} and higher than reported SC potential windows of SCs based in cobalt compounds (1.4 V)³⁰ and cadmium compounds (*ca.* 1.4 V)³¹ active electrode materials. Indeed, this high operation potential window leads to the achievement of high-energy storage density values as will be discussed later. One of the key criteria for the performance of an SC is the self-discharge characteristics.⁸ Self-discharge is the spontaneous decrease in the voltage of the charged SCs with time under open-circuit conditions. It is very important to suppress this phenomenon, which will enable SCs to store energy more efficiently.⁸ The $\text{CdCO}_3/\text{CdO}/\text{Co}_3\text{O}_4/\text{Ni}/\text{AC}$ SC device showed a self-discharging rate (final voltage/initial voltage) of *ca.* 13.5% after 22 hours (see Fig. S7†).

The electrochemical performance and the electrochemical events occurring within the electrodes of the supercapacitor were further investigated using electrochemical impedance spectroscopy (EIS) analysis. EIS measurements for the $\text{CdCO}_3/\text{CdO}/\text{Co}_3\text{O}_4/\text{Ni}/\text{AC}$ SC devices have been performed using a sinusoidal signal in the frequency range from 0.1 Hz to 100 kHz at open circuit potential, and the corresponding Nyquist plot for a typical SC sample is shown in Fig. 4. A nearly straight line was observed in the low-frequency range and a small semicircle in the high-frequency region. The straight line represents the Warburg impedance, which indicates the diffusive impedance of electrolyte ions in the $\text{CdCO}_3/\text{CdO}/\text{Co}_3\text{O}_4$ composite (diffusive resistance of electrolyte ions in the interior cavities of the electrode), and the semicircle diameter of EIS is assigned to the charge-transfer resistance (R_{ct}), while the intersection between the curve and the x -axis indicates the resistance of equivalent series (R_s).^{5,25,29,32,33} Moreover, that small semicircle indicates both the pseudocapacitive nature of the composite material and higher charge transfer rates.³⁴ The Nyquist plots were then fitted with an equivalent electrical circuit (see inset of Fig. 4) and the interpreted data are shown in Table 1. The fit indicated by a solid line in the plot showed good agreement with the data. This confirmed the suitability of the equivalent circuit model used. The total SC impedance can be accurately modeled as serial and parallel combinations of different circuit components (see inset of Fig. 4): a serial resistance R_s denoting the electrolyte solution resistance and a parallel combination constituted by R_{ct} charge transfer resistance, constant phase shift elements (CPE_1 and CPE_2) and a Warburg impedance (W_0). An electrolyte solution serial resistance $R_s = 0.62 \Omega$ was obtained (see Table 1), indicating the very good quality of the interfacial contact between the composite electrode and the electrolyte. The R_{ct} charge transfer resistance exhibited a value of 4.32Ω as can be seen in Table 1. Low R_s and R_{ct} values indicate the low internal resistance, good ion accessibility, rapid faradaic redox reactions, and high electrochemical reversibility in the low-frequency region due to the nano-structure of the composite.³² Moreover, as a result of the EIS simulation fitting process, two CPE parameters were obtained: a constant-phase element CPE_1 to simulate double-layer capacitance (AC/NF electrode interface), and a pseudo-capacitance CPE_2 of the material redox process ($\text{CdCO}_3/\text{CdO}/\text{Co}_3\text{O}_4/\text{NF}$ electrode interface).²⁶ The corresponding CPE parameters (Q constant phase element with power α , see note of Table 1),³⁵ were extracted. A Warburg impedance element (or diffusion constant) appeared in the equivalent circuit, providing information about the ionic diffusion within the SC.²⁵ The Warburg W_0 impedance is a function of three parameters: W - R , the Warburg diffusion impedance; W - T , the diffusion time constant, and W - P , the phase factor ($0 < W-P < 1$).³⁶ The values achieved by these Warburg parameters (see Table 1), indicate short ionic routes and good capacitive efficiency, similar to that exhibited by other metallic carbonate-based supercapacitors.²⁵ The W - P value of 0.9 indicates a material with a high degree of porosity.²⁵

The electrochemical device performance of the SC was evaluated by galvanostatic charge/discharge (GCD) analysis (at



various current densities and an operating potential window from 0 to 1.5 V), as illustrated in Fig. 5a. The nearly symmetric GCD curves demonstrated the good reversibility of the charge–discharge process.³⁷ The GCD curves did not show the plateaus that are characteristic of a battery, nor were they totally linear, which confirmed the pseudocapacitance characteristics of the compound, indicating that we are facing a hybrid SC, which is consistent with the CV curves that show the absence of redox peaks (see Fig. 3). On increasing the imposed current density value (see inset of Fig. 5a), the GCD curves continued to show a relative symmetrical profile, demonstrating the good reversibility of the charge–discharge process and low polarization of the active material, thus giving high specific capacitance values. This could be due to the high specific surface area exhibited by the cubic micro-particles of the CdCO₃/CdO/Co₃O₄ composite electrode (see Fig. 2). This micro-structure allows the electrolyte to go into the nanopores (formed between the cubic micro-particles), leading to a greater accumulation of electrical charge and improved electrical transport due to the interconnectivity that exists between the micro-cubes. The obtained specific capacitance value (excluding the *IR* drop) is *ca.* 84 F g^{−1} @ 1 mA cm^{−2} GCD current density, which is comparable to, or even higher than recent reports for other ASSCs, such as CuO//AC (72.4 F g^{−1}),³⁸ MnO₂//graphite (72.7 F g^{−1})³⁹ and Co₃O₄//AC (57.4 F g^{−1}).⁴⁰ Detailed specific capacitance values at other different GCD current densities are depicted in Table S3.† This obtained high capacitance value can be explained by a synergistic interaction between the CdCO₃, CdO, and Co₃O₄ single phases of the studied composite, leading to an increase in the specific capacitance of the only CdCO₃ single-phase (results of an exhaustive study of this synergistic effect on the final performance of the composite SC device are now being prepared and will be published). Fig. 5b shows the rate discharge capability of the CdCO₃/CdO/Co₃O₄@Ni//AC supercapacitor device at different current densities. It can be seen that the specific capacitance decreases with the increase in the current density. This is in line with the general law of the rate performance of electrochemical energy storage devices and may be associated with ion-exchange processes.^{32,41,42} It is difficult for the diffusion of ions to reach the entire electrode material at high current density values.^{32,41,42} Fig. 5b also shows the coulombic efficiency of the SC device as a function of the current density. There was a slight decrease in this coulombic efficiency from *ca.* 90% to *ca.* 85% at low and high current density values, respectively, indicating that the reversibility of the charge–discharge process decreases with the increase of the current density values.

As is known, the performance of an SC is dependent on the intrinsic properties of active electrode materials.⁹ In the present case, the specific capacitance of the CdCO₃/CdO/Co₃O₄@Ni//AC SC device (being higher than those exhibited by conventional AC-based symmetric SCs, *i.e.* ~20 F g^{−1}), is on the one hand restricted by the AC negative electrode (~165 F g^{−1}), and in the other hand is significantly improved by the pseudocapacitance of the CdCO₃/CdO/Co₃O₄@Ni electrode (1057 F g^{−1} @ 1 mA cm^{−2} GCD current density, see Table S3† for the capacitance value at other different GCD current density values).

One of the most crucial factors for the practical application of SC devices is long cycle life. Therefore, the cycling stability test was conducted with the hybrid SC device at a current density of 30 mA cm^{−2}, and the obtained plot is displayed in Fig. 6. The hybrid SC demonstrated excellent cycling stability (from an initial specific capacitance of 84.0 F g^{−1}), with a capacitance retention of *ca.* 92% after 6000 continuous charge–discharge cycles. The capacitance retention increased after the 200 cycles (as can be seen in Fig. 2c), which is likely due to an “activation process”.^{2,7,43} Further, from the 4000th cycle to the 6000th one, a slight decrease in the capacitance retention can be seen, arriving at *ca.* 92% at the end of the GCD cycling. The electrochemical charge and discharge processes can generate crystal imperfections at the level of the composite cubic-shaped micro-particles, and then a higher porosity of the composite electrode can be achieved. This allows the diffusion of OH[−] ions inside the active material within the formed nanopores, favoring the hydration of the bulk oxides (Co₃O₄ and CdO) supported on the CdCO₃ matrix, diminishing the charge transfer resistance. It also demonstrates that cadmium carbonate can serve as a support and give high stability to the electrode, as other studies have shown,²³ since many of the electrodes for hybrid transition metal SCs need a support of graphene oxide or CNT in order to have high cycling stability. On assembling two SCs in series, and after charging them for only 10 s at 3 V, the device could efficiently power 5 mm blue (2.5 V, 2 mA) round light-emitting diode (LED) indicators, see inset of Fig. 6. For instance, a red LED remained very bright after 15 min as displayed in Fig. S8.† Moreover, these SCs can drive a mini rotation motor (operating current and voltage 8 mA and 0.18 V, respectively) strongly after 90 s of the charging step (see Movie in ESI†).

To demonstrate the overall electrochemical properties of the assembled device, the Ragone plot of the CdCO₃/CdO/Co₃O₄@Ni//AC SC device (energy density (*E*) *vs.* power density (*P*)) is presented in Fig. 7, *E* and *P* values of the SC device were calculated from a double electrode system (see eqn (2) and (3)). Here, the SC device achieved an excellent energy density of 26.3 W h kg^{−1} at a power density of 51 W kg^{−1}, which is comparable to, or even higher than, that of many previously reported supercapacitors such as CoO/Co₃O₄//AC,³⁰ Co₃O₄//AC,⁴⁴ MnCo₂O₄ based SC,⁴⁵ PPy/Go/MnOx//AC,⁴⁶ 3D rGO-based SC,⁴⁷ MoS₂/NiCo(OH)₂CO₃//AC²⁵ and Co₃O₄@Co₂(CO₃)(OH)₂//AC²⁷ (see Fig. 7). This indicates the promising and practicable application of the CdCO₃/CdO/Co₃O₄@Ni//AC SC device for energy storage fields.

4 Conclusions

A CdCO₃/CdO/Co₃O₄@NF SC electrode has been prepared through direct growth without additives or binders *via* a facile hydrothermal-annealing method. This composite electrode has been effectively used as a positive electrode for hybrid SCs with an AC-based negative electrode. The as-assembled devices demonstrated a high specific capacitance of 84 F g^{−1} @ 1 mA cm^{−2} with a maximum energy density of 26.3 W h kg^{−1} and a power density of 2290 W kg^{−1} along with a widespread



potential window of 1.5 V and long cycle life (92% after 6000 cycles). The as-assembled SCs (connected in series) were also employed to power various light-emitting diodes and move an electrical mini-motor. The excellent electrochemical properties demonstrate the promising potential applications of the $\text{Co}_3\text{O}_4/\text{CdO}/\text{CdCO}_3@\text{NF}$ in energy storage devices.

Conflicts of interest

There are no conflicts to declare.

Acknowledgements

The authors are grateful to “Programa Operativo FEDER Andalucía of Spain through the project UMA18-FEDERJA-039”; CSIC/UdelaR, Montevideo and PEDECIBA-Física, Uruguay; PUCV DI Consolidado 039.377/2021 project and ANID 21170121 PhD scholarship, Chile.

References

- 1 Y. Yu, H. Wang, H. Zhang, Y. Tan, Y. Wang, K. Song, B. Yang, L. Yuan, X. Shen and X. Hu, *Electrochim. Acta*, 2020, **334**, 135559.
- 2 C. Zhou, Y. Zhang, Y. Li and J. Liu, *Nano Lett.*, 2013, **13**, 2078–2085.
- 3 J. Ge, J. Wu, L. Fan, Q. Bao, J. Dong, J. Jia, Y. Guo and J. Lin, *J. Energy Chem.*, 2018, **27**, 478–485.
- 4 J. Rodríguez-Moreno, E. Navarrete-Astorga, E. A. Dalchiale, R. Schrebler, J. R. Ramos-Barrado and F. Martín, *Chem. Commun.*, 2014, **5652**, 5652–5655.
- 5 S. M. Cha, S. Chandra Sekhar, R. Bhimanaboina and J. S. Yu, *Inorg. Chem.*, 2018, **57**, 8440–8450.
- 6 P. Xu, J. Liu, T. Liu, K. Ye, K. Cheng, J. Yin, D. Cao, G. Wang and Q. Li, *RSC Adv.*, 2016, **6**, 28270–28278.
- 7 B. Wu, H. Qian, Z. Nie, Z. Luo, Z. Wu, P. Liu, H. He, J. Wu, S. Chen and F. Zhang, *J. Energy Chem.*, 2020, **46**, 178–186.
- 8 C. Breitkopf and K. Swider-Lyons, *Springer Handbook of Electrochemical Energy*, 2017.
- 9 B. Pandit, L. K. Bommeneedi and B. R. Sankapal, *J. Energy Chem.*, 2019, **31**, 79–88.
- 10 S. M. Chen, R. Ramachandran, V. Mani and R. Saraswathi, *Int. J. Electrochem. Sci.*, 2014, **9**, 4072–4085.
- 11 Z. Fan, J. Yan, T. Wei, L. Zhi, G. Ning, T. Li and F. Wei, *Adv. Funct. Mater.*, 2011, **21**, 2366–2375.
- 12 K. Tao, P. Li, L. Kang, X. Li, Q. Zhou, L. Dong and W. Liang, *J. Power Sources*, 2015, **293**, 23–32.
- 13 X. H. Xia, J. P. Tu, Y. Q. Zhang, Y. J. Mai, X. L. Wang, C. D. Gu and X. B. Zhao, *J. Phys. Chem. C*, 2011, **115**, 22662–22668.
- 14 J.-Y. Kim, K.-H. Kim, H.-K. Kim, S.-H. Park, K. C. Roh and K.-B. Kim, *ACS Appl. Mater. Interfaces*, 2015, **7**, 16686–16693.
- 15 C.-H. Xu, P.-Y. Shen, Y.-F. Chiu, P.-W. Yeh, C.-C. Chen, L.-C. Chen, C.-C. Hsu, I.-C. Cheng and J.-Z. Chen, *J. Alloys Compd.*, 2016, **676**, 469–473.
- 16 S. Dhibar, P. Bhattacharya, G. Hatui and C. K. Das, *J. Alloys Compd.*, 2015, **625**, 64–75.
- 17 P. Sivakumar, M. Jana, M. Kota, M. G. Jung, A. Gedanken and H. S. Park, *J. Power Sources*, 2018, **402**, 147–156.
- 18 A. Adán-Más, T. M. Silva, L. Guerlou-Demourgues, L. Bourgeois, C. Labrugere-Sarroste and M. F. Montemor, *J. Power Sources*, 2019, **419**, 12–26.
- 19 S. Ramesh, S. Khandelwal, K. Y. Rhee and D. Hui, *Composites, Part B*, 2018, **138**, 45–54.
- 20 J. Mei, T. Liao, G. A. Ayoko, J. Bell and Z. Sun, *Prog. Mater. Sci.*, 2019, **103**, 596–677.
- 21 J. Chang, V. V. Todkar, R. S. Mane, D. Ham, T. Ganesh and S.-H. Han, *Phys. E*, 2009, **41**, 1741–1745.
- 22 S. Deng, X. Xiao, G. Chen, L. Wang and Y. Wang, *Electrochim. Acta*, 2016, **196**, 316–327.
- 23 S. Devaraj, H. Y. Liu and P. Balaya, *J. Mater. Chem. A*, 2014, **2**, 4276–4281.
- 24 M. A. Garakani, S. Abouali, B. Zhang, C. A. Takagi, Z.-L. Xu, J. Huang, J. Huang and J.-K. Kim, *ACS Appl. Mater. Interfaces*, 2014, **6**, 18971–18980.
- 25 A. Y. Chen, H. H. Liu, P. Qi, X. F. Xie, M. T. Wang and X. Y. Wang, *J. Alloys Compd.*, 2021, **864**, 158144.
- 26 Y. Zhong, X. Cao, Y. Liu, L. Cui and J. Liu, *J. Colloid Interface Sci.*, 2021, **581**, 11–20.
- 27 P. Sheng, S. Tao, X. Gao, Y. Tan, W. Dajun, B. Qian and P. Chu, *J. Mater. Sci.*, 2020, **55**, 12091–12102.
- 28 L. Cao, F. Xu, Y.-Y. Liang and H.-L. Li, *Adv. Mater.*, 2004, **16**, 1853–1857.
- 29 H. Xuan, T. Liang, G. Zhang, Y. Guan, H. Li, R. Wang, P. Han and Y. Wu, *J. Alloys Compd.*, 2020, **818**, 153350.
- 30 M. Pang, G. Long, S. Jiang, Y. Ji, W. Han, B. Wang, X. Liu, Y. Xi, D. Wang and F. Xu, *Chem. Eng. J.*, 2015, **280**, 377–384.
- 31 P. Xu, J. Liu, P. Yan, C. Miao, K. Ye, K. Cheng, J. Yin, D. Cao, K. Li and G. Wang, *J. Mater. Chem. A*, 2016, **4**, 4920–4928.
- 32 M. Karuppaiah, R. Akilan, P. Sakthivel, S. Asaithambi, R. Shankar, R. Yuvakkumar, Y. Hayakawa and G. Ravi, *J. Energy Storage*, 2020, **27**, 101138.
- 33 X. He, R. Li, J. Liu, Q. Liu, R. chen, D. Song and J. Wang, *Chem. Eng. J.*, 2018, **334**, 1573–1583.
- 34 M. Jana, J. S. Kumar, P. Khanra, P. Samanta, H. Koo, N. C. Murmu and T. Kuila, *J. Power Sources*, 2016, **303**, 222–233.
- 35 E. Navarrete-Astorga, D. Solís-Cortés, J. Rodríguez-Moreno, E. A. Dalchiale, R. Schrebler, F. Martín and J. R. Ramos-Barrado, *Chem. Commun.*, 2018, **54**, 10762–10765.
- 36 R. OrjHaková, H. Wiemhöfer, J. Paulsdorf, V. Barinková, A. Bednáriková and R. M. Smith, *J. Solid State Electrochem.*, 2006, **10**, 458–464.
- 37 C. Zhu, Y. He, Y. Liu, N. Kazantseva, P. Saha and Q. Cheng, *J. Energy Chem.*, 2019, **35**, 124–131.
- 38 S. E. Moosavifard, M. F. El-Kady, M. S. Rahmanifar, R. B. Kaner and M. F. Mousavi, *ACS Appl. Mater. Interfaces*, 2015, **7**, 4851–4860.
- 39 M. Huang, X. L. Zhao, F. Li, L. L. Zhang and Y. X. Zhang, *J. Power Sources*, 2015, **277**, 36–43.
- 40 W. Liu, X. Li, M. Zhu and X. He, *J. Power Sources*, 2015, **282**, 179–186.
- 41 X. Chen, Q. Su, J. Yu, M. Wei, G. Guo and Y. Wang, *RSC Adv.*, 2021, **11**, 25170–25178.



- 42 S. He, C. Zhang, C. Du, C. Cheng and W. Chen, *J. Power Sources*, 2019, **434**, 226701.
- 43 I. Rathinamala, I. M. Babu, J. J. William, G. Muralidharan and N. Prithivikumaran, *Mater. Sci. Semicond. Process.*, 2020, **105**, 104677.
- 44 Y. Hao, H. Wang, Z. Hu, L. Gan and Z. Xu, *New J. Chem.*, 2015, **39**, 68–71.
- 45 J. Gomez and E. E. Kalu, *J. Power Sources*, 2013, **230**, 218–224.
- 46 C. H. Ng, H. N. Lim, Y. S. Lim, W. K. Chee and N. M. Huang, *Int. J. Energy Res.*, 2015, **39**, 344–355.
- 47 S. Madani, C. Falamaki, H. Alimadadi and S. H. Aboutalebi, *J. Energy Storage*, 2019, **21**, 310–320.

